

# Simulation and Experimental Analysis of Aerogel's Attenuation for High-Energy Alpha Particles in Fission-Fusion Fragment Rocket Applications

Sandeep Puri\*<sup>1</sup>, Andrew Gillespie<sup>1</sup>, Ian Jones<sup>1</sup>, Cuikun Lin<sup>1</sup>, Ryan Weed\*<sup>2</sup>, Robert V. Duncan\*<sup>1</sup>

<sup>1</sup>Center for Emerging Energy Sciences, Department of Physics and Astronomy, Texas Tech University, Lubbock, Texas, USA

<sup>2</sup>Positron Dynamics, Livermore, CA

\* **Correspondence:**

[sandpuri@ttu.edu](mailto:sandpuri@ttu.edu); [ryan.weed@positrondynamics.com](mailto:ryan.weed@positrondynamics.com); [robert.duncan@ttu.edu](mailto:robert.duncan@ttu.edu);

## 1. Abstract

Emerging studies are geared toward exploring new methods of nuclear rocket propulsion to provide more efficient space transit beyond Earth's orbit<sup>[1], [2]</sup>. One method is to employ a Fission Fragment Rocket Engine (FFRE) utilizing fissionable layers embedded in a low-density aerogel<sup>[3]</sup>. A quantitative understanding of particle attenuation is necessary to develop a working prototype that permits the fission fragments to escape the layers and contribute to the specific impulse rather than being attenuated and contributing to waste heat. In this study, the Monte Carlo n-Particle transport code (MCNP 6.2) was utilized to theoretically investigate the attenuation of alpha particles from Am-241 sources within aerogel materials. Simulations explored aerogels of varied densities and various carbonaceous and silicon-based materials. The simulations were used to predict the anticipated alpha particle intensity reaching a detector. Columbia Resin No. 39 (CR-39) was used as a Plastic Nuclear Track Detector (PNTD) and was employed to experimentally analyze the particle attenuation by the aerogels.

**Keywords: Aerogel, high energy alpha particle, nuclear rocket, propulsion, plastic nuclear track detector**

## 2. Introduction

A human spaceflight mission poses significant challenges and risks to the crew's health. Hazards like ionizing space radiation, extreme gravitational changes, and prolonged isolation and confinement are among the dangers astronauts encounter<sup>[4], [5]</sup>. It's crucial to minimize these risks for a successful mission. Enhancing travel efficiency and speed stands as a potential solution to tackle these challenges. This could involve reducing mission duration, which necessitates a rocket equipped with both high thrust (necessary for escaping planetary gravity) and high impulse (essential for achieving rapid interplanetary travel)<sup>[6]</sup>. Nuclear rocket propulsion offers the promise of greater thrust and higher impulse compared to traditional chemical rockets<sup>[7]</sup>. This advancement could enable faster, more efficient journeys to distant planets (like Mars) and facilitate the transportation of scientific equipment or materials for use in space far beyond Earth's orbit.

In existing nuclear propulsion models, fission fragments are absorbed within the nuclear fuel, producing heat. Traditional nuclear rocket reactors then create thrust by heating a gas and expelling it via a nozzle<sup>[8]</sup>. This technique, however, is indirect and not very efficient. Fission fragments, heavy parts of a nuclear core that undergoes a fission reaction, typically carry over 80% of the total released energy. With high atomic mass, a substantial charge state, and extremely high velocity, they're ideal propellants for a magnetic thrust nozzle. Unfortunately, these fission fragments quickly lose speed within solid matter. To make a FFRE work, the fragments need to be released from a very thin layer or a fuel particle that is much smaller than the attenuation length scale ( $<10 \mu\text{m}$ ). These tiny fuel particle elements must also be rigidly contained and accumulated in a very low-density structure to reach a critical mass of fissile fuel, enabling the initiation and sustenance of a nuclear chain reaction. The main challenge in developing a viable FFRE concept lies in meeting both criticality and allowing fission fragment escape. Chapline<sup>[2]</sup> conceived the FFRE and proposed a solution by rotating micron-thick enriched fuel plates through a moderator structure and extracting the fission fragment via a magnetic yoke. Another concept<sup>[9]</sup> suggested suspending a cloud of fissile dust particles within a moderator and magnet structure. However, these ideas faced significant engineering obstacles, including manufacturing fuel elements, thermal and mechanical constraints, and unmanageable launch mass.

Recent breakthroughs in ultra-low-density aerogel materials<sup>[10]</sup> have introduced the possibility of utilizing a solid substance to capture and assemble these micron-sized fuel particles into a critical assembly. The aerogel's remarkably low density prevents substantial attenuation of fission fragments within the core while also providing effective cooling for the fuel particles through high infrared and visible light transmission. Typically ranging in densities from  $0.01$  to  $0.4 \text{ g/cm}^3$ , aerogels boast extensive total specific surface areas of  $30$  to  $600 \text{ m}^2/\text{g}$ . The discovery of aerogel is attributed to Kistler in 1931, who developed these materials by eliminating the solvent from a liquid component through processes like lyophilization (freeze-drying) or critical point drying. This results in a highly porous, lightweight, and interconnected material<sup>[11]</sup>. However, a quantitative understanding of the attenuation ratio of aerogel to nuclear particles remains an ongoing area of study.

Alternatively, a CR-39 PNTD may be used to experimentally detect a range of particles with high sensitivity. Capable of effectively detecting protons with energies up to  $14 \text{ MeV}$ , alpha particles with energies up to  $100 \text{ MeV}$ , and heavy ions across various energy levels, it serves as a versatile detector. Moreover, it can identify neutrons spanning energies from  $500 \text{ keV}$  to  $20 \text{ MeV}$  by observing an enlarged latent damage trail or "track." Details about the discovery and sensitivity of CR-39 detector are present in a number of previous studies<sup>[12]-[17]</sup>.

Monte Carlo is a widely adopted statistical technique used for obtaining numerical solutions to physical or mathematical problems, especially when obtaining direct physical measurements proves challenging or unfeasible. In scenarios involving the transport of a large number of charged particles, Monte Carlo relies on random numbers and probability distributions to estimate crucial composite particle characteristics, including energy, position, direction, path-length, and the types of physical interactions experienced within a medium. This technique is capable of determining particle fluence across surfaces or cells and quantifying energy deposition

within defined volumes. Numerous Monte Carlo packages such as MCNP<sup>[18]</sup>, FLUKA<sup>[19]</sup>, OPENMC<sup>[20]</sup>, etc. have been developed specifically to address radiation transport problems. Among these, MCNP 6.2 facilitates the handling of diverse particle transport and interactions across a broad energy spectrum and in three-dimensional arbitrary geometries. It is developed at Los Alamos National Laboratory (LANL), USA and accessible through Oak Ridge National Laboratory (ORNL). It treats particle interactions as either continuous or discrete energies, utilizing cross-section data from the ENDF libraries<sup>[21]</sup>.

In this study, MCNP 6.2 was utilized to theoretically investigate the attenuation of alpha particles from Am-241 sources, while CR-39 PNTD was employed for experimental aerogel attenuation analysis. Various densities and thicknesses of aerogel were also examined in the research.

### 3. Simulation and experiments

#### 3.1 Simulation

MCNP 6.2 simulations were employed to predict the anticipated alpha particle intensity reaching a detector. Our next phase involves optimizing an aerogel layer, aiming to permit the transmission of alpha particles through the layer with little or no attenuation. Initially, the transmission rates of 5.5-MeV alpha particles through various aerogel materials were evaluated: silicon dioxide (SiO<sub>2</sub>), graphite oxide (C<sub>2</sub>O), and simulated graphene (represented as elemental carbon). The preliminary study focused on determining the alpha particle transmission rates through these aerogel compositions. **Figure 1** illustrates the simulation's basic geometry, involving a surface source, aerogel layer, and a tally zone utilized for assessing the percentage of transmitted alpha particles. Each layer consisted of cylinders of slightly different dimensions. The surface source was given a radius of 2 cm and a height of 1 cm. Each of these dimensions were arbitrarily chosen because the source zone was only defined in order to visualize the positions and double check the geometry within MCNP. Since the front surface was used as the surface source, the thickness of this region is irrelevant. The aerogel and tally zone radii were set to 2.1 cm. These radii were chosen to be slightly larger than the source radius because this increases the calculation efficiency. The front surface of the source was positioned 1 mm away from the aerogel and the tally zone was separated from the aerogel by 0.1 mm. The source zone and tally zone were filled with argon. All other regions were filled with air. The first set of simulations was performed for an aerogel consisting of SiO<sub>2</sub>. A set of simple simulations were performed using a 1 mm-thick cylinder of "aerogel" which is just SiO<sub>2</sub> in MCNP. There is a small air gap between the source and the aerogel as well as another small air gap between the aerogel and the tally zone. The percentage of alpha particles transmitted through the aerogel were monitored by dividing the "tracks entering" the tally zone by the "tracks entering" the aerogel. Consecutively the F4 tally (track length estimates of the particle flux) within the tally zone were also monitored.

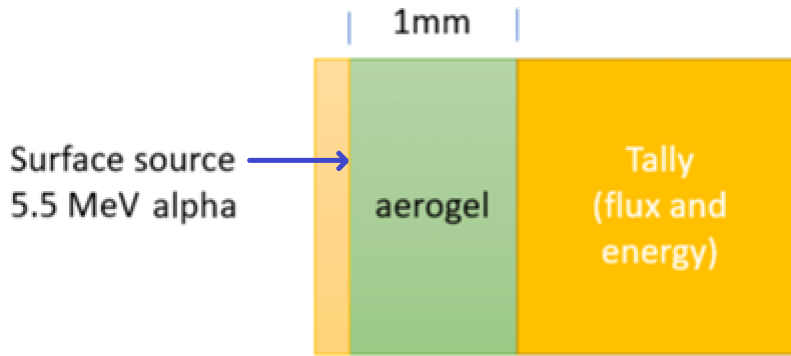


**Figure 1:** The simplified geometry used for simulating alpha particles incident on an aerogel sample of either  $\text{SiO}_2$ ,  $\text{C}_2\text{O}$ , or  $\text{C}$  of varied densities.

### 3.2 Experiment

The experiments utilized silicon (Si) and graphene aerogels, having approximate densities of  $0.14 \text{ g/cm}^3$  and  $0.0125 \text{ g/cm}^3$ , respectively. These tests incorporated a CR39 PNTD and an Am-241-point source with a radioactivity level of about  $0.88 \text{ } \mu\text{Ci}$ . Am-241 source emits alpha ( $\alpha$ ) particles with an energy of about 5.5 MeV. Dr. Ryan Weed from Positron Dynamics in San Francisco, CA, provided both the Am-241-point source and the Si aerogel. The graphene aerogel, labeled G-AREOGEL-75, was acquired from Graphene Supermarket, with an advertised density of around  $0.0125 \text{ g/cm}^3$  (source: Graphene Supermarket). Additionally, the CR39 detector used in these experiments was synthesized at TTU.

To conduct the experiment, a 3D-printed holder was created to secure the Am-241 source and a lead shield containing an aperture with a specified diameter (2.45 mm) and a marked scale for reference. This setup facilitated the positioning of the CR39 detector, as depicted in **Figures 2(a)** and **(c)**. Different areas of the CR39 detector were exposed to the americium source for varying durations – specifically, 1, 5, and 10 minutes – to gather data. The experiment comprised four configurations: one without any aerogel layer between the source and the detector (direct exposure), and others with aerogel layers of different compositions, densities, and thicknesses between the source and the detector (as depicted in **Figures 2(b)** and **3(b)**). Subsequent to data collection, the exposed samples underwent etching in a 6.25 molar NaOH solution at  $80 \text{ } ^\circ\text{C}$  for 30 minutes. This etching process enhances particle tracks by attacking and breaking the polymer structure through hydroxide ions, swiftly etching away the majority of the plastic along the paths influenced by  $\alpha$ -particle interactions.

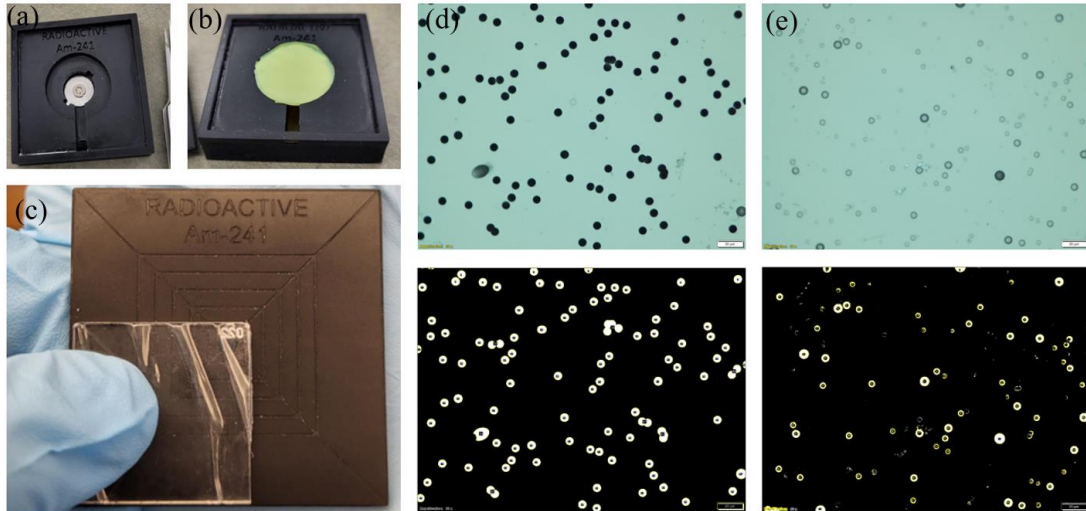


**Figure 2:** (a) A 3D-printed holder housing Am-241, (b) A 0.22 mm-thick layer of Si-aerogel positioned above Am-241, and (c) A 3D-printed lead featuring an aperture and a marked scale for reference, facilitating precise exposure control on the CR39 detector. (d) The upper panel displays an image showing  $\alpha$  tracks on the CR39, exposed to Am-241 for 1 minute without any intervening aerogel layer. The lower panel exhibits a processed image utilizing ImageJ software<sup>[22], [23]</sup>, resulting in a particle count of 96. (e) The upper panel showcases an image portraying  $\alpha$  tracks on the CR39, exposed to Am-241 for 60 minutes with a 0.22 mm-thick Si-aerogel layer in between. The lower panel displays a processed image utilizing ImageJ software, indicating a particle count of 72.

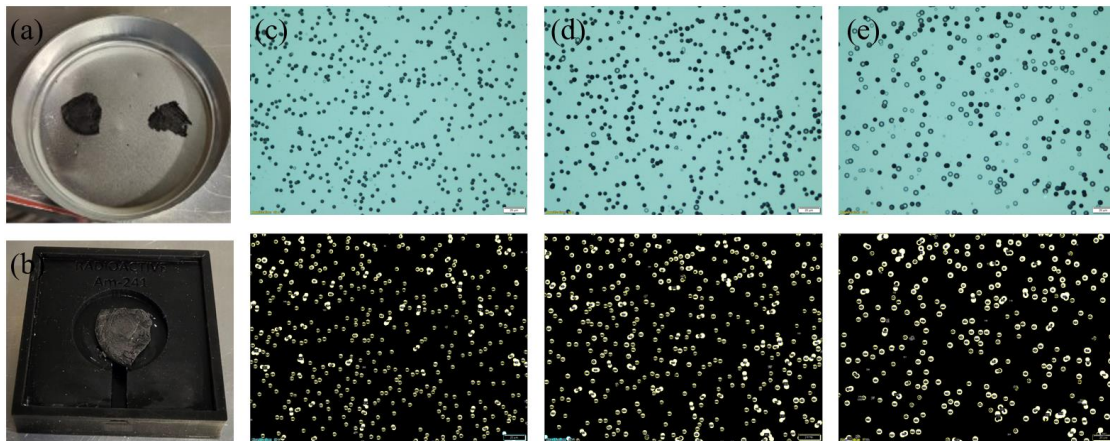


**Figure 3:** (a) Graphene aerogel slices with thicknesses of 1.6 mm (left) and 0.9 mm (right), (b) experimental setup illustrating the positioning of graphene aerogel atop Am-241, (c) the upper panel displays  $\alpha$  tracks on CR39, exposed to Am-241 for 5 minutes without an intervening aerogel layer, while the lower panel exhibits a processed image using ImageJ software, indicating a particle count of 430. (d) The upper panel shows  $\alpha$  tracks on CR39 exposed to Am-241 for 5 minutes with a 0.9 mm-thick graphene aerogel layer in between, and the lower panel, processed image

using ImageJ software, indicates a particle count of 392. (e) The upper panel presents  $\alpha$  tracks on CR39 exposed to Am-241 for 5 minutes with a 1.6 mm-thick graphene aerogel layer in between, while the lower panel displays a processed image using ImageJ software, indicating a particle count of 305.

Following the etching process, the detector samples underwent microscopic examination, and images were captured for detailed analysis and particle estimation in specific regions<sup>[24]</sup>. These captured images were subsequently processed using ImageJ software. Initially, the images were converted into binary format, rendering them as black and white images that highlighted particle tracks as white circular spots, as depicted in the lower panel of **Figures 2:** (d), (e), and **Figure 3:** (c), (d), (e). The software automatically counted these spots, providing an estimation of the number of particles within the designated region. To ensure accuracy, each region exposed to the source for a specific duration (e.g., 1 minute) was examined at five distinct sites. The software-derived particle count from each site was averaged to obtain a more precise estimation of the particle number. A detailed summary of the analyzed data is presented comprehensively in **Table 1**.

#### 4. Results and Discussions

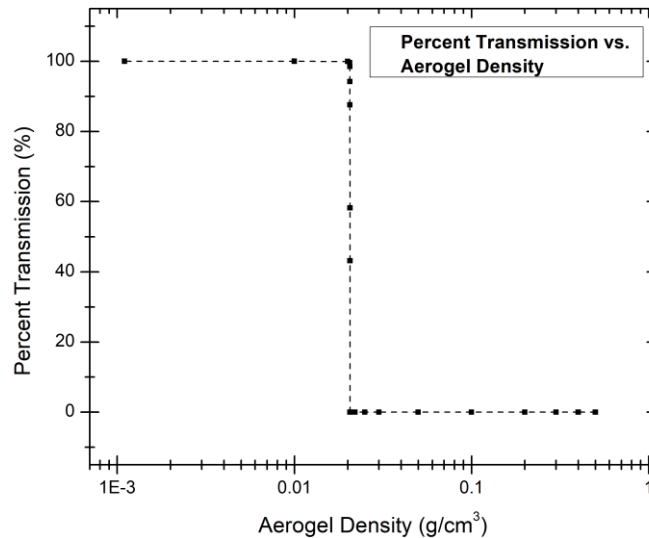


**Figure 4:** The percentage of transmitted 5.5-MeV alpha particles as a function of SiO<sub>2</sub> aerogel density.

According to the MCNP simulation outcomes depicted in **Figure 4**, a distinct and very abrupt decrease in alpha particle transmission is observed when utilizing a density around 0.02 g/cm<sup>3</sup>. Nearly all particles are transmitted for aerogel densities below this threshold, while nearly all particles are attenuated for densities above this value. The transition occurs at densities close to  $0.0206 \pm 0.0001$  g/cm<sup>3</sup>, as illustrated in **Figure 4**. Further, the influence of aerogel density on alpha particle attenuation was explored. Initially, our assessment of the aerogel density provided for preliminary experiments measured approximately 0.15 g/cm<sup>3</sup>, while the manufacturer's claim suggested a density close to 0.090 g/cm<sup>3</sup>. These simulations assumed the aerogel composition to

be 100% SiO<sub>2</sub>. They were straightforward simulations involving a 5.5 MeV alpha particle surface source, an aerogel zone, and a subsequent tally zone. Subsequent simulations were conducted to determine alpha particle transmission rates through aerogels made from alternative materials: Graphite Oxide (C<sub>2</sub>O) and Graphene Aerogel (C). Interestingly, the maximum density allowing for approximately 100% transmission of alpha particles remained consistent across different aerogel materials. This initial observation aligns with our experimental findings.

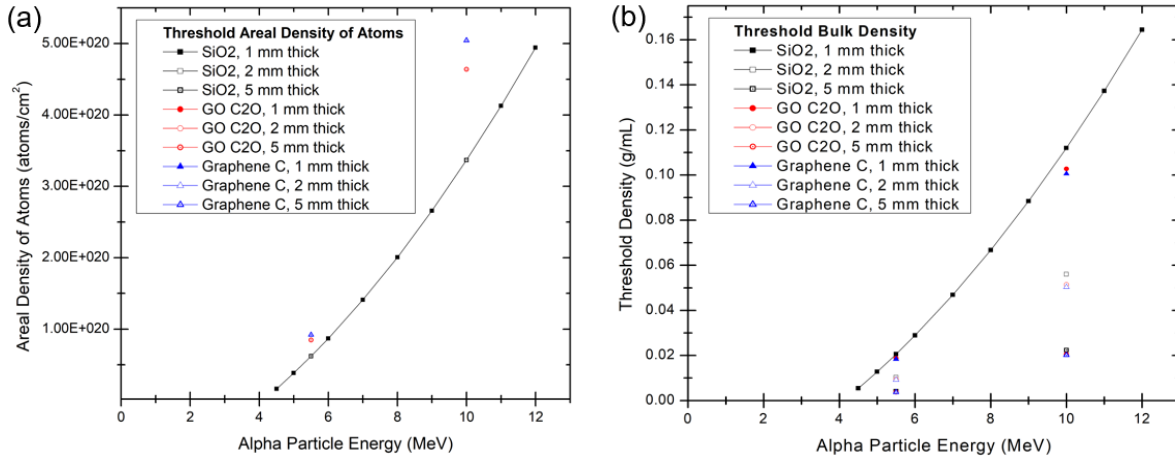


**Figure 5:** *Left:* The threshold areal density of atoms above which aerogels cease permitting alpha particles to be transmitted. *Right:* The threshold bulk density above which aerogels cease permitting alpha particles to be transmitted.

Based on the simulations, the transition from complete to no attenuation of alpha particles occurs precisely at 0.02 g/cm<sup>3</sup>, independent of the aerogel composition, for alpha particles emitted at the Am241 decay energy (~5 MeV). To delve further into this, simulations were performed with three aerogel materials, varying alpha energy and aerogel thicknesses. When aerogels are below the threshold density, they permit nearly 100% of incident alpha particles to be transmitted through to the following layer. This transmission rate drops drastically for densities above the threshold value. The areal density is defined as the number of atoms per square centimeter in the direction of the incident alpha particle. The bulk density is defined as the mass of the aerogel divided by its volume. At a given energy of incident alpha particles, these three materials have a threshold areal density that is similar to one another, as shown in the left panel of **Figure 5**. For 5.5-MeV incident alpha particles, the threshold areal density of atoms is between 6 - 9 x10<sup>19</sup> atoms/cm<sup>2</sup>. This threshold areal density of atoms differs more for incident higher energies. For 10-MeV incident alpha particles, the threshold areal density of atoms is between 3 - 5 x10<sup>20</sup> atoms/cm<sup>2</sup>.

Since, at a given incident particle energy, the threshold areal density of atoms for one material is the same regardless of the aerogel thickness, it is necessary for the threshold bulk density to vary. If a thicker aerogel is used, then more atoms will occupy each square centimeter in the path of the incident alpha particles. As the thickness increases, it is necessary for the threshold bulk density to decrease, as shown in the right panel of **Figure 5**.

The simulation outcomes align closely with the experimental findings detailed in **Table 1**. Using a 0.22 mm SiO<sub>2</sub> aerogel with a density of 0.09 g/cm<sup>3</sup>—exceeding the threshold—nearly all

alpha particles are attenuated. Conversely, employing 12.5 mg of graphene aerogel results in an average attenuation of 31.4% for a thickness of 1.6 mm and 12.3% for a thickness of 0.9 mm.

**Table 1:** Data collected from the experiment for particle counts for different set up.

Aerogel thickness & composition	Exposure time	No. of particles per minute	Transmission ratio	Attenuation ratio
(mm)	(min)	(n/min)		
0	1	103.4		
0	1	121.0		
	5	83.4		
	10	63.3		
0.22 (SiO <sub>2</sub> )	1	2.0	0.019	0.981
	10	0.8	0.008	0.992
	30	0.5	0.005	0.995
	60	1.2	0.012	0.988
0.9 (graphene)	1	107.0	0.884	0.116
	5	72.6	0.871	0.129
1.6 (graphene)	1	77.8	0.643	0.357
	5	59.6	0.715	0.285
	10	44.3	0.699	0.301

At the threshold areal density below which the aerogel becomes transparent to 5.5 MeV alpha particles, around  $6.0 \times 10^{19}$  atoms/cm<sup>2</sup>, the area per atom is  $1.7 \times 10^{-20}$  cm<sup>2</sup>. This implies an average diameter of about 1.3 angstroms (Å) per atom ( $1.3 \times 10^{-10}$  m/atom). The typical size of the Si atom is around 2.0 Å and the oxygen atom is around 1.5 Å, but these lengths are estimated for atoms in free space, and this size per atom is dependent on the type of bonding (ionic or covalent) within the crystal in which it is located. Though the size of the SiO<sub>2</sub> molecule can span a large range dependent on its crystalline structure or amorphous character, the average diameter per atom at the threshold areal density is close to the diameter of the individual atoms in free space. One would expect these ions to be slightly smaller inside this aerogel structure. It is feasible that the aerogel loses its transparency when the areal density of the atoms fully blocks off any ‘free space’ between the atoms, as seen by the incoming alpha particle. In the aerogel structure, as in any solid binding of the Si and O atoms, the Si and O atoms have a somewhat positive charge, since they donate electrons to their binding structure. The alpha particle at 5.5 MeV is very small, with a deBroglie wavelength of only 6.1 fm ( $6.1 \times 10^{-15}$  m). The frequent grazing collisions do not significantly affect the transport of alpha particles because they result in steady small energy losses as the alpha particles propagate through the aerogel. However, the paths of alpha particles are blocked when they suffer ‘hard’ collision with the nucleus of the Si or O ion, and experiences most of the core ionic repulsion of the atom’s bare nucleus. Though the positively charged alpha particle and atomic Si / O nuclei repel one another slightly in the low areal density limit, when the areal density of the Si / O completely blocks the alpha particle’s path, then the aerogel suddenly becomes opaque to the alpha particles. The deBroglie wavelength of the alpha particle decreases inversely



proportional to the square root of its kinetic energy, so its wavelength decreases as the particle energy increases. This permits it to ‘wedge in’ more effectively between the atoms as its energy increases. Further, the diameter of a carbon atom ranges from 1.5 Å in a covalent solid, to 0.6 Å in an ionic solid, so it is smaller than both the Si and O atoms. Hence, one would expect the carbon-rich aerogels (C<sub>2</sub>O and graphene) to have a higher threshold aerial density for these 5.5 MeV alpha particles, and indeed they do. This effect becomes much more pronounced at higher alpha particle energies, as the simulations show in **Figure 5**.

## 5. Conclusions

This research presents a comprehensive investigation into the aerogel's attenuation ratio for high-energy alpha particles, employing advanced MCNP simulation techniques and experimental analyses. Simulations based on silicon, graphene oxide, and pure graphene aerogels with variations in areal density, bulk density, and thickness, demonstrated a transition from complete attenuation to no attenuation at 0.02 g/cm<sup>3</sup> for alpha particles emitted at the Am-241 decay energy (~5MeV). Further simulations indicated a consistent threshold areal density of atoms regardless of material thickness for a given incident alpha particle energy. Increasing aerogel thickness necessitates a decrease in bulk density to maintain the same threshold areal density. Additionally, the threshold areal density exhibited a slight increase with rising incident alpha energy. The findings from simulations align closely with experimental results, which showed that utilizing 0.22 mm SiO<sub>2</sub> aerogels with a density of 0.09 g/cm<sup>3</sup>, which is above threshold, resulted in almost complete alpha particle attenuation. Conversely, the use of 12.5 mg/cm<sup>3</sup> graphene aerogel demonstrated an average attenuation of 31.4% at a thickness of 1.6 mm and an average attenuation of 12.3% at a thickness of 0.9 mm. This study has enhanced our understanding of aerogel behavior in alpha particle attenuation, offering valuable insights for diverse applications and help us explore the feasibility of utilizing the aerogels to capture and assemble the micron-sized fuel particles into a critical assembly for our proposed FFRE.

## 6. References

- [1] R. Weed, R. V. Duncan, M. Horsley, and G. Chapline, “Radiation characteristics of an aerogel-supported fission fragment rocket engine for crewed interplanetary missions,” *Front. Space Technol.*, vol. 4, p. 1197347, Sep. 2023, doi: 10.3389/frspt.2023.1197347.
- [2] G. Chapline, “Fission fragment rocket concept,” *Nuclear Instruments and Methods in Physics Research Section A: Accelerators, Spectrometers, Detectors and Associated Equipment*, vol. 271, no. 1, pp. 207–208, Aug. 1988, doi: 10.1016/0168-9002(88)91148-5.
- [3] R. Weed, *Aerogel Core Fission Fragment Rocket Engine*. [Online]. Available: <https://www.nasa.gov/general/aerogel-core-fission-fragment-rocket-engine/>
- [4] Z. S. Patel *et al.*, “Red risks for a journey to the red planet: The highest priority human health risks for a mission to Mars,” *npj Microgravity*, vol. 6, no. 1, p. 33, Nov. 2020, doi: 10.1038/s41526-020-00124-6.
- [5] L. J. Abadie, C. Nathan, L. Charles W., S. Mark J., and T. Jennifer L., “The Human Body in Space,” NASA, 2021, [Online]. Available: <https://www.nasa.gov/hrp/bodyinspace>
- [6] “Ideal Rocket Equation,” NASA, 2021, [Online]. Available: <https://www.grc.nasa.gov/www/k-12/rocket/rktpow.html>
- [7] R. Raju, “Beyond the Solid Core Nuclear Thermal Rocket: A Computational Investigation into Criticality and Neutronics Performance of Advanced Liquid and Gas Core Reactor Approaches for Next Generation Performance,” 2022, doi: 10.7302/6019.
- [8] P. R. McClure, “Space Nuclear Reactor Development,” LA--UR-17-21904, 1345964, Mar. 2017. doi: 10.2172/1345964.
- [9] R. Clark and R. Sheldon, “Dusty Plasma Based Fission Fragment Nuclear Reactor,” in *41st AIAA/ASME/SAE/ASEE Joint Propulsion Conference & Exhibit*, Tucson, Arizona: American Institute of Aeronautics and Astronautics, Jul. 2005. doi: 10.2514/6.2005-4460.
- [10] M. Tabata, I. Adachi, Y. Ishii, H. Kawai, T. Sumiyoshi, and H. Yokogawa, “Development of transparent silica aerogel over a wide range of densities,” *Nuclear Instruments and Methods in Physics Research Section A: Accelerators, Spectrometers, Detectors and Associated Equipment*, vol. 623, no. 1, pp. 339–341, Nov. 2010, doi: 10.1016/j.nima.2010.02.241.
- [11] S. S. Kistler, “Coherent Expanded Aerogels and Jellies,” *Nature*, vol. 127, no. 3211, pp. 741–741, May 1931, doi: 10.1038/127741a0.
- [12] P. J. Potts, “Nuclear techniques for the determination of uranium and thorium and their decay products,” in *A Handbook of Silicate Rock Analysis*, Boston, MA: Springer US, 1987, pp. 440–471. doi: 10.1007/978-1-4615-3270-5\_13.

- [13] K. O. Inozemtsev and V. V. Kushin, “Comparative analysis of CR-39 sensitivity for different sets of measurable track parameters,” *Radiation Measurements*, vol. 91, pp. 44–49, Aug. 2016, doi: 10.1016/j.radmeas.2016.04.010.
- [14] S. Kodaira *et al.*, “A performance test of a new high-surface-quality and high-sensitivity CR-39 plastic nuclear track detector – TechnoTrak,” *Nuclear Instruments and Methods in Physics Research Section B: Beam Interactions with Materials and Atoms*, vol. 383, pp. 129–135, Sep. 2016, doi: 10.1016/j.nimb.2016.07.002.
- [15] M. Fujii, R. Yokota, and Y. Atarashi, “New polymeric track detectors of high sensitivity (SR-86),” *International Journal of Radiation Applications and Instrumentation. Part D. Nuclear Tracks and Radiation Measurements*, vol. 15, no. 1–4, pp. 107–110, 1988, doi: 10.1016/1359-0189(88)90110-0.
- [16] V. K. Mandrekar, G. Chourasiya, P. C. Kalsi, S. G. Tilve, and V. S. Nadkarni, “Nuclear track detection using thermoset polycarbonates derived from pentaerythritol,” *Nuclear Instruments and Methods in Physics Research Section B: Beam Interactions with Materials and Atoms*, vol. 268, no. 5, pp. 537–542, Mar. 2010, doi: 10.1016/j.nimb.2009.11.015.
- [17] M. A. Rana, “How to achieve precision and reliability in experiments using nuclear track detection technique?,” *Nuclear Instruments and Methods in Physics Research Section A: Accelerators, Spectrometers, Detectors and Associated Equipment*, vol. 592, no. 3, pp. 354–360, Jul. 2008, doi: 10.1016/j.nima.2008.04.025.
- [18] “<https://mcnp.lanl.gov/>; <https://silverfirsoftware.com/>”, [Online]. Available: <https://mcnp.lanl.gov/>; <https://silverfirsoftware.com/>
- [19] G. Battistoni *et al.*, “Overview of the FLUKA code,” *Annals of Nuclear Energy*, vol. 82, pp. 10–18, Aug. 2015, doi: 10.1016/j.anucene.2014.11.007.
- [20] P. K. Romano, N. E. Horelik, B. R. Herman, A. G. Nelson, B. Forget, and K. Smith, “OpenMC: A state-of-the-art Monte Carlo code for research and development,” *Annals of Nuclear Energy*, vol. 82, pp. 90–97, Aug. 2015, doi: 10.1016/j.anucene.2014.07.048.
- [21] M. B. Chadwick *et al.*, “ENDF/B-VII.1 Nuclear Data for Science and Technology: Cross Sections, Covariances, Fission Product Yields and Decay Data,” *Nuclear Data Sheets*, vol. 112, no. 12, pp. 2887–2996, Dec. 2011, doi: 10.1016/j.nds.2011.11.002.
- [22] T. Ferreira and W. S. Rasband, *ImageJ User Guide IJ 1.46*. [Online]. Available: [imagej.nih.gov/ij/docs/guide/](http://imagej.nih.gov/ij/docs/guide/)
- [23] C. A. Schneider, W. S. Rasband, and K. W. Eliceiri, “NIH Image to ImageJ: 25 years of image analysis,” *Nat Methods*, vol. 9, no. 7, pp. 671–675, Jul. 2012, doi: 10.1038/nmeth.2089.
- [24] Olympus IMS, “Instructions BX53M System Microscope,” [Online]. Available: [https://www.olympus-ims.com/en/.downloads/download/?file=285218737&fl=en\\_US](https://www.olympus-ims.com/en/.downloads/download/?file=285218737&fl=en_US)

## 7. Supplementary Materials

### 1. CR39 Synthesis.

CR39 is synthesized through the polymerization of allyl diglycol carbonate (ADC) in the presence of an initiator, such as diisopropyl peroxydicarbonate (IPP) or benzoyl peroxide (BPO). In our process, we utilized 2,5,8-Trioxanonanedioic acid di-2-propenyl ester as the CR39 monomer and BPO as the initiator for polymerization.

#### 1.1 Materials and equipment used for synthesis:

1. 2,5,8-Trioxanonanedioic acid di-2-propenyl ester (CR39 monomer),
2. Benzoyl peroxide (BPO),
3. glass plates,
4. Teflon gasket
5. syringes,
6. Teflon beaker,
7. Teflon stirrer capsule,
8. hotplate cum magnetic stirrer,
9. oven, and
10. Vacuum degasser.

#### 1.2 Procedure for CR39 synthesis:

Take 100 g of CR39 monomer in a Teflon beaker. Add 5 wt.% of BPO into the beaker containing the monomer. Place the beaker on the hot-plate and set the temperature to 40 °C. Turn on the magnetic stirrer and let the BPO mix/dissolve for 30-60 min. Meanwhile, pre-heat the oven to 80 °C. Prepare a mold using two glass plates clamping together and seal with a 1.75 mm thick Teflon gasket. When the BPO is completely dissolved in the mixture, degas the mixture under vacuum then pour into a mold carefully using a syringe. After the mixture is poured into the mold, place the mold in the oven, standing vertically. Keep the mold at 80 °C for 2 h and cure it for another 2 h at 100 °C. Depending on the amount of mixture used, curing time might vary. Once the polymerization is complete, take the mold out of the oven and remove the clamp. The CR39 is now ready.

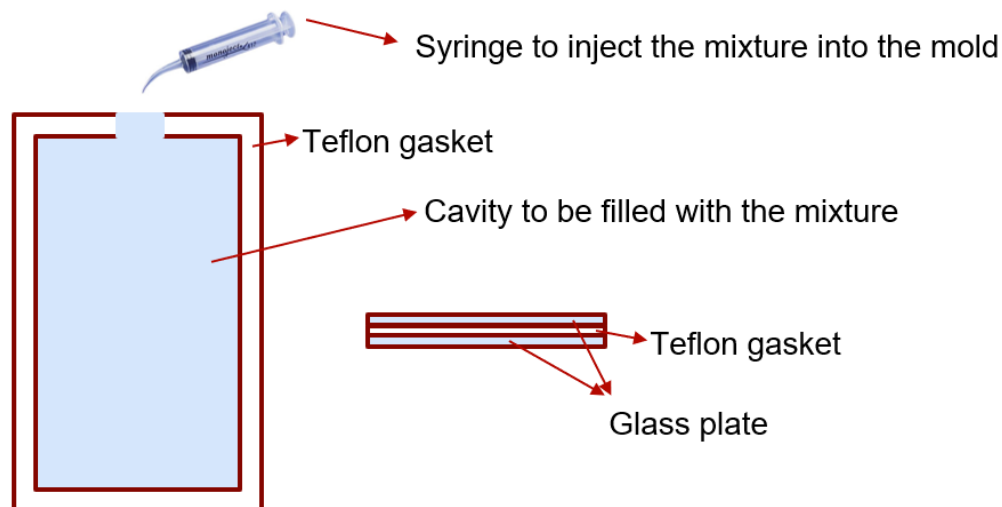


**Figure 1:** Schematic of mold prepared for CR39 polymerization.

## 2. Etching:

When the CR39 is exposed to a radioactive material, the emitted energetic particles colliding with the polymer structure leaves a trail of broken chemical bonds within the CR39. In order to analyze the particle tracks it is necessary to etch the plastic to visualize the tracks. The CR39 is immersed in concentrated alkali solution, the hydroxide ions in the solution attacks and break the polymer structure, etching away the bulk of the plastic. The attack and breaking of the polymer are more rapid along the paths of damage left by charged particle interaction.

In our experiment, the CR39 plastic was exposed to Am-241 which emits alpha particles with energy  $\sim 5.5$  MeV. After the exposure, we etched the plastic using 6.25 Molar NaOH solution at 90 °C for 30 min. The etching solution was prepared by adding 25 g of NaOH into 100 ml water. The solution was preheated to 90 °C before immersing the CR39 into it. After 30 min the plastic is taken out of the solution and washed with flowing water for 1 – 5 min. The plastic is then dried and observed under the microscope.